Geoscience Frontiers xxx (xxxx) xxx

HOSTED BY

ELSEVIER

Contents lists available at ScienceDirect

Geoscience Frontiers

journal homepage: www.elsevier.com/locate/gsf

Reaction between basaltic melt and orthopyroxene at 3.0–4.5 GPa: Implications for the evolution of ocean island basalts in the mantle

Chunjuan Zang [a,b,c], Mingliang Wang [a,b,c,d,*], Hongfeng Tang [b], Hanqi He [b]

[a] School of Resource and Civil Engineering, Suzhou University, Suzhou 234000, Anhui, China
[b] Key Laboratory for High Temperature & High Pressure Study of the Earth's Interior, Institute of Geochemistry, Chinese Academy of Science, Guiyang 550002, China
[c] Key Laboratory of Mine Water Resource Utilization, Education Department of Anhui Province, Suzhou 234000, China
[d] School of Earth and Environment, Anhui University of Science and Technology, Huainan 232001, Anhui, China

ARTICLE INFO

Keywords:
Ocean island basalt (OIB)
Melt–pyroxenite reaction
Mineral–melt distribution coefficients
Trace elements
Experimental petrology

ABSTRACT

Interactions between basaltic melt and orthopyroxenite (Opx) were investigated to gain a better understanding of the consequences of the residence and transport of ocean island basalts (OIBs) within the mantle. The experiments were conducted using a DS-3600 six-anvil apparatus at 3.0–4.5 GPa and 1300–1450 °C. The basaltic melt and Opx coexisted at local equilibrium at these pressures and temperatures; the initial melts dissolved Opx, which modified their chemical composition, and clinopyroxene (Cpx) precipitated with or without garnet (Grt). The trace-element contents of Grt, Cpx, and melt were measured and the mineral–melt distribution coefficients (*D*) of Cpx–melt and Grt–melt were calculated, which can be used to assess the distribution of trace elements between basalt and minerals in the mantle. Two types of reaction rim were found in the experimental products, Cpx, and Cpx + Grt; this result indicates that residual rocks within the mantle should be pyroxenite or garnet pyroxenite. Both rock types are found in mantle xenoliths from Hawaii, and the rare-earth-element (REE) pattern of Cpx in these mantle pyroxenites matches those of Cpx in the experimental reaction rims. Furthermore, residual melts in the experimental products plot in similar positions to Hawaiian high-SiO_2 OIBs on major-element Harker diagrams, and their trace-element patterns show the signature of residual Grt, particularly in runs at ≤1350 °C and 4.0–4.5 GPa. Trace-element concentrations of the experimental residual melts plot in similar positions to the Hawaiian OIBs on commonly used discrimination diagrams (Ti vs. Zr, Cr vs. Y, Cr vs. V, Zr/Y vs. Zr, and Ti/Y vs. Nb/Y). These results indicate that reaction between basaltic melt and pyroxenite might contribute to the generation of Hawaiian high-SiO_2 OIBs and account for their chemical variability.

1. Introduction

Ocean island basalts (OIBs) provide important records of the composition of the mantle and Earth's evolution (Hofmann and White, 1982; Ren et al., 2009). Their major- and trace-element and isotope compositions vary widely (Hofmann and White, 1982; Zindler and Hart, 1986; Hauri, 1996; Sobolev et al., 2005, 2007; Niu, 2009; Ren et al., 2009; Liu and Ren, 2013; Huang and Zheng, 2017), and it is thought that much of this variability is related to heterogeneity of the OIBs source region. It has been proposed that OIBs are generated by: (1) partial melting of recycled oceanic crust (Hofmann and White, 1982; Sobolev et al., 2000, 2005, 2007); (2) partial melting of a mixture of oceanic crust and continental crust (or a component with geochemical characteristics similar to those of the continental crust) (Zindler and Hart, 1986; Dan and O'Nions, 1995; Hofmann, 1997); or (3) very low-degree partial melting of the mantle, or partial melting of mantle contaminated by a low-degree melt (Niu, 2009). All three hypotheses are consistent with the generation of OIBs by partial melting of heterogeneous peridotites, pyroxenites, and amphibolites (see Liu and Ren, 2013, and references therein). Most of the explanations for the variability of OIBs focus on their source origin, and until recently it was thought that OIBs rise rapidly within the mantle with only minor assimilation. However, an increasing number of studies have shown that assimilation can change the chemical composition of OIBs (Hilton et al., 1995; Borisova et al., 2002, 2017; Genske et al., 2013). Field observations (Garcia and Presti, 1987; Caroff et al., 1995; Tegner et al., 2005) and experimental

* Corresponding author. School of Resource and Civil Engineering, Suzhou University, Suzhou 234000, Anhui, China.
E-mail address: wangapple1999@126.com (M. Wang).
Peer-review under responsibility of China University of Geosciences (Beijing).

https://doi.org/10.1016/j.gsf.2020.05.023
Received 16 October 2019; Received in revised form 13 April 2020; Accepted 21 May 2020
Available online xxxx

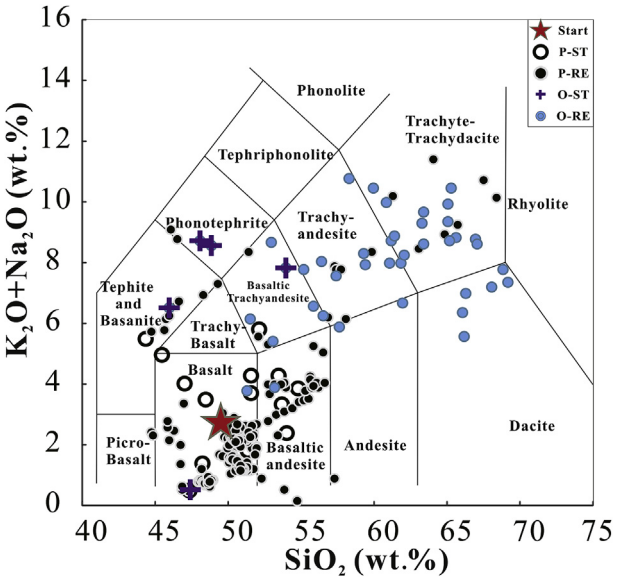

Fig. 1. Petrographic classification of reacted melts produced by reaction between basaltic melt and peridotite or pyroxenite. Start: starting composition of basalt used in this study. P-ST and P-RE: starting basalt and reacted melts, respectively, in basalt–peridotite experiments (Yaxley and Green, 1998; Falloon and Danyushevsky, 2000; Lambart et al., 2009, 2012; Tominaga et al., 2009; Wang et al., 2010, 2013, 2016; Van Den Bleeken et al., 2011; Mallik and Dasgupta, 2012; Gao et al., 2017). O-ST and O-RE: starting basalt and reacted melts, respectively, in basalt–pyroxenite experiments (Shaw et al., 1998). These reacted melts varied widely compared with their starting basalts on this petrographic classification diagram.

investigations of reactions between basaltic melt and peridotite or pyroxenite over timescales as short as 3 h (Shaw et al., 1998; Morgan and Liang, 2005; Tominaga et al., 2009; Wang et al., 2013; Gao et al., 2017) confirm that even relatively short durations of contact between basalt and the surrounding rock at high temperatures (>1100 °C) can modify the composition of basalt substantially, and that the composition might be modified further by longer durations of reaction during magma residence and transport.

However, although the effects of reaction between basalt and the surrounding rock can be recognised, it is difficult to constrain the details of reaction from field observations alone because of the following: (1) The primary magma is rarely preserved, and samples collected in the field typically show evidence of interaction between melt and peridotite and/or pyroxenite; (2) the effects of pressure (*P*) and temperature (*T*) on the reactions are difficult to assess because field samples might have undergone multiple cycles of interaction between melt and peridotite and/or pyroxenite at different *P*-*T* conditions; and (3) the residual minerals generated by interactions between melt and peridotite and/or pyroxenite are difficult to confirm, with mantle xenoliths being found at the surface in OIBs but most residual minerals remaining in the mantle. In contrast, laboratory experiments where the *P*, *T*, and initial melt composition can be controlled and used to derive a detailed understanding of the melt–rock interactions that contribute to the generation of OIBs.

A number of experiments have been performed to study the interactions between basaltic melt and mantle rocks, and most of these have focused on basalt–peridotite reactions (Yaxley and Green, 1998; Falloon and Danyushevsky, 2000; Morgan and Liang, 2005; Shaw and Dingwell, 2007; Lambart et al., 2009, 2012; Tominaga et al., 2009; Wang et al., 2010, 2013, 2016; Van Den Bleeken et al., 2011; Gao et al., 2017), because peridotite is regarded as the most common rock type within the mantle. Typical experiments involve reaction of natural or synthetic basaltic melt compositions with harzburgite or lherzolite at 1 atm to 5.0 GPa and 1100–1650 °C (Fig. 1). The experimental products cover the compositional range from basalt to dacite. These existing results can be used to understand major-element variations and the influences of *P* and *T* on melt–peridotite reactions. Tominaga et al. (2009) described the trace-element characteristics of experimental basaltic melts, which

Table 1
Chemical composition of starting materials.

	Basalt (DG-3)	OIB	OIB (Iceland)	OIB (Hawaii)	MORB	Opx (DMP-01)
Major element (wt.%)						
SiO_2	48.52	–	48.00	48.10	50.50	54.46
TiO_2	3.88	–	1.32	2.33	1.68	0.17
Al_2O_3	12.82	–	15.00	12.60	14.70	4.38
FeO	13.76	–	10.50	11.50	10.40	6.3
MnO	0.19	–	0.18	0.18	0.18	0.11
MgO	4.50	–	9.90	10.50	7.60	33.49
CaO	9.57	–	12.30	10.50	11.40	0.63
Na_2O	1.92	–	1.88	2.26	2.79	0.17
K_2O	0.88	–	0.19	0.51	0.16	0.01
P_2O_5	0.38	–	0.14	0.30	0.18	0.18
NiO	N.A.	–	–	–	–	N.A.
Cr_2O_5	N.A.	–	–	–	–	0.35
LOI	1.64	–	–	–	–	–
Total	98.06	–	99.41	98.78	99.59	100.25
Mg#	0.31	–	0.57	0.56	0.51	0.91
Trace element (ppm)						
Li	N.A.	5.6	–	–	–	1.63
Be	N.A.	–	–	–	–	0.03
Sc	N.A.	0.387	40.4	27.8	39.8	14.8
V	440	–	276	273	309	90.5
Cr	N.A.	–	477	556	249	1906
Co	49.2	–	–	–	–	59.0
Ni	65.8	–	192	299	92	827
Cu	469	–	119	93	74	17.3
Zn	175	–	81	117	91	39.0
Ga	28.7	–	14.9	18.4	17.5	3.53
Rb	37.2	31	6.2	10.6	2.88	0.02
Sr	549	660	170	423	129	0.20
Y	40.4	29	20.8	25.3	36.8	0.98
Zr	318	280	72	144	117	1.53
Nb	41.5	48	9.7	20	5.24	0.00
Mo	2.27	2.4	–	–	–	0.04
Ag	0.70	–	–	–	–	0.01
Cd	0.33	–	–	–	–	0.04
Sn	6.35	2.7	–	–	–	1.25
Sb	0.36	0.03	–	–	–	0.02
Cs	0.92	–	–	–	–	0.01
Ba	475	350	54	234	29.2	0.02
La	43	37	6.2	18	5.21	0.00
Ce	101	80	15.1	38	14.9	0.01
Pr	12.9	9.7	2.1	5.1	2.24	0.00
Nd	56.6	38.5	9.8	23.1	12	0.02
Sm	12.6	10	2.7	5.82	3.82	0.03
Eu	3.23	3	1.01	1.96	1.36	0.01
Gd	10.9	7.62	3.21	5.84	4.99	0.05
Tb	1.59	1.05	0.55	0.88	0.9	0.01
Dy	8.97	5.6	3.4	4.93	6.08	0.12
Ho	1.73	1.06	0.7	0.91	1.28	0.04
Er	4.14	2.62	1.99	2.29	–	0.13
Tm	0.58	0.35	0.293	0.308	3.79	0.03
Yb	3.60	2.16	1.89	1.81	3.63	0.24
Lu	0.49	0.3	0.288	0.257	0.53	0.05
Hf	10.3	7.8	2.22	3.52	2.79	0.05
Ta	3.07	2.7	0.79	1.43	0.34	0.00
W	3.18	0.56	–	–	–	0.00
Tl	0.11	0.077	–	–	–	0.01
Pb	14.3	3.2	0.93	1.46	0.57	0.03
Bi	1.43	–	–	–	–	0.01
Th	7.48	4	0.64	1.61	0.404	0.00
U	1.92	1.02	0.23	0.41	0.119	0.00

Note: Total Fe as FeO. Mg# = molar MgO/(Mg + ΣFeO). N.A.: no analysis. '-': data not provided in the cited references. The trace-element composition of OIB is from Sun and Mcdonough (1989); the average major- and trace-element compositions of OIB (Iceland), OIB (Hawaii), and MORB are from Huang and Zheng (2017) and references therein. The major- and trace-element composition of Opx (DMP-01) is from Wang et al. (2019).

Table 2
Summary of experimental conditions and results.

No.	Temperature (°C)	Opx/Gl Ratio[a]	Pressure (GPa)	Duration (h)	Phase Assemblage
ZS-06	1300	2:1	3.0	48	Opx + Gl + ***Cpx(r)+Grt(r)***
ZS-07	1350	2:1	3.0	48	Opx + Gl + ***Cpx(r)+Grt(r)***
ZS-08	1400	2:1	3.0	48	Opx + Gl + ***Cpx(r)***
ZS-10	1300	2:1	4.0	48	Opx + ***Cpx*** + ***Grt(r)***
ZS-11	1350	3:1	4.0	48	Opx + Gl + ***Cpx(r)+Grt(r)***
ZS-12	1400	3:2	4.0	48	Opx + Gl + ***Cpx(r)***
ZS-13	1450	3:2	4.0	48	Opx + Gl + ***Cpx(r)***
ZS-14	1350	3:2	4.5	45	Opx + Gl + ***Cpx(r)+Grt***(r)
ZS-21	1300	1:1	4.0	60	Opx + Gl + ***Cpx(r)+Grt(r)***

Gl: glass (quenched melt), Opx: orthopyroxene, Grt: garnet, Cpx: clinopyroxene, (r): mineral in reaction rim, [a]: weight-based Opx/Gl ratio.

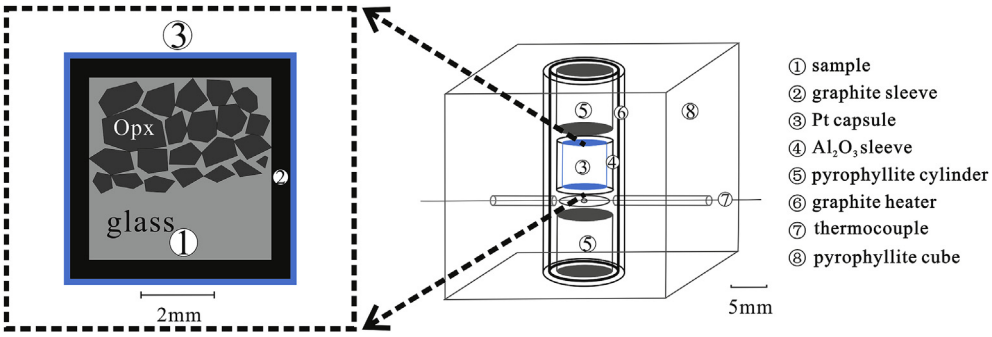

Fig. 2. Sketch map of experimental assembly (after Wang et al., 2019).

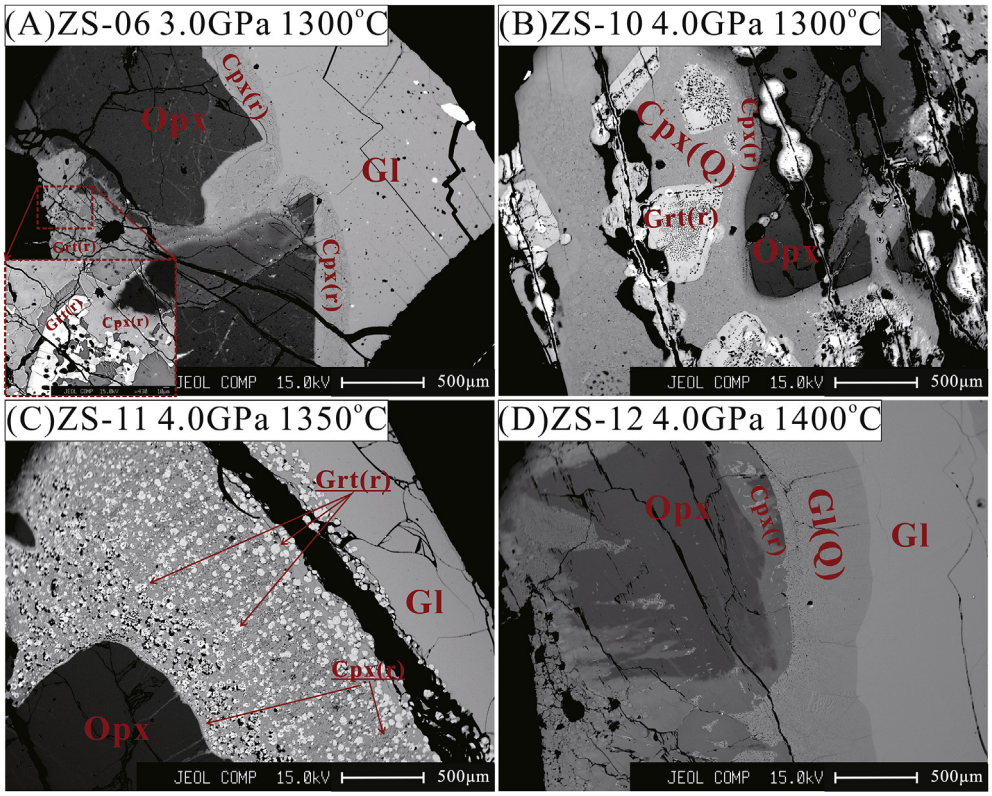

Fig. 3. Representative BSE photomicrographs of experimental products. Gl: Glass (melt); Opx: orthopyroxene; Grt: garnet; Cpx: clinopyroxene; (r): mineral in reaction rim; (Q): quenched melt. There are two kinds of reaction rims in reaction products, Cpx + Grt in runs at ≤1350 °C and Cpx in runs at >1350 °C.

provided further insights into the evolution of OIBs. Meanwhile, pyroxenites are also known to contribute to the generation of OIBs, Hauri (1996) showed that Hawaiian OIBs are enriched in SiO_2 at a given FeO concentration, indicating that these OIBs equilibrated with garnet-bearing pyroxenites. This result is consistent with the NiO concentrations of olivine (Ol) from Hawaiian OIBs (Sobolev et al., 2005, 2007). Although there are fewer pyroxenites than peridotites in lithospheric mantle, but pyroxenites may great contribute to the generation of

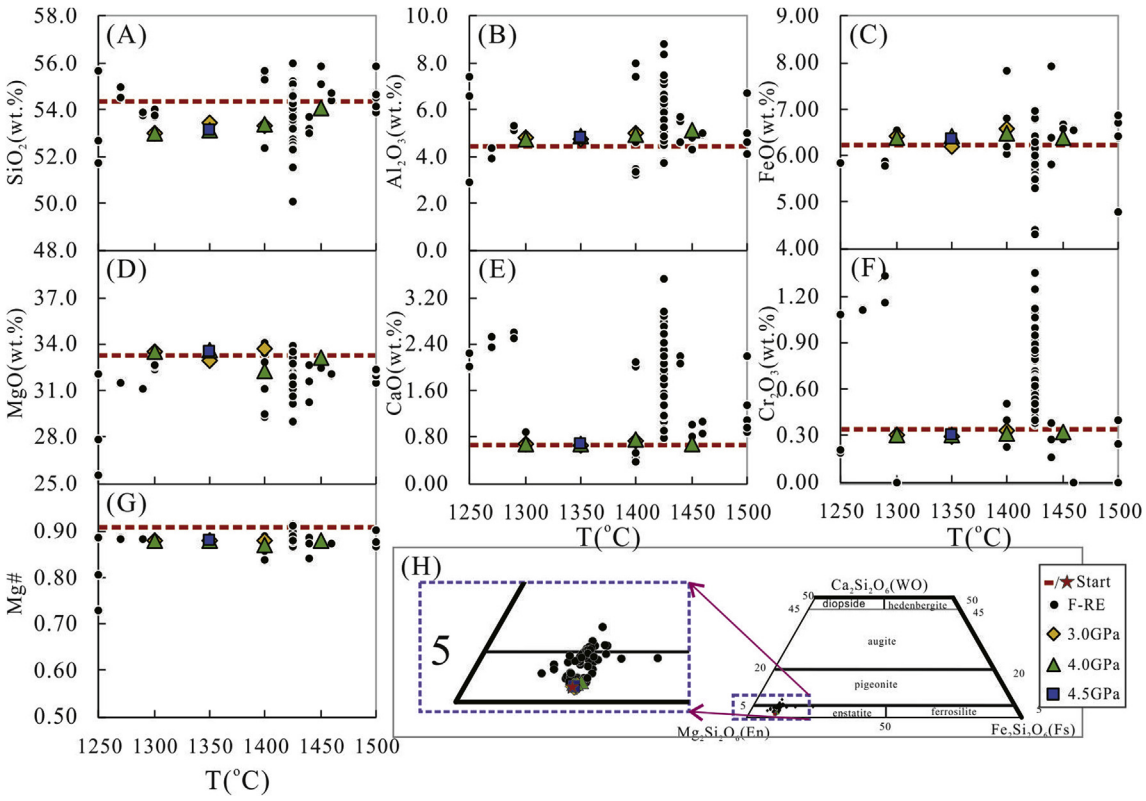

Fig. 4. Plots of major-element oxide concentrations and the Mg# of residual Opx in experimental products. Start: composition of starting Opx. F-RE: Opx in basalt–peridotite experiments at 1250–1500 °C (Yaxley and Green, 1998; Lambart et al., 2009, 2012; Wang et al., 2010, 2013; Mallik and Dasgupta, 2012; Gao et al., 2017). 3.0 GPa, 4.0 GPa, 4.5 GPa: results from runs in this study at 3.0 GPa, 4.0 GPa, and 4.5 GPa, respectively. The schematic diagram of pyroxene classifications is from Morimoto (1988). The major element composition of residual Opx in this study are almost same to the starting one, which is consistent with the Opx in basalt–peridotite experiments (Yaxley and Green, 1998; Mallik and Dasgupta, 2012; Gao et al., 2017) but different from the ones in dissolution experiments (Wang et al., 2013, 2016).

OIBs in some area, such as Hawaii. According to the result from Sobolev et al. (2005), more than 50% of OIBs located in Hawaii formed during past 1 million years may have very close relationship with melt-pyroxene equilibrium, indicating that the basalt–pyroxenites reactions may play a key role in the generation of OIBs and need to be study carefully. However, few studies have documented basalt–pyroxenite interactions, in contrast to the large number of studies of basalt–peridotite interactions. Shaw et al. (1998) simulated basalt–pyroxenite interactions experimentally at 1 atm and 1190 and 1220 °C. Their results show that the reacted melts and the Hawaiian high-SiO_2 OIBs are enriched in SiO_2 to a similar extent. However, the results of Shaw cannot be used to understand mantle processes directly because: (1) the pressure of the experiments was much lower than those of reactions in the mantle, and the reaction pressure might affect the stability of residual minerals such as garnet, with consequences for the chemical composition of the reacted melts; and (2) trace-element concentrations were not provided for the reacted melt, which restricts interpretation of the results in the context of OIB evolution. Existing experimental results do not address two critical aspects of the reaction between basaltic melt and pyroxenite during the generation and evolution of OIBs: (1) the relationship between reaction *P–T* (equivalent to reaction depth and geothermal gradient) and the residual mineral assemblage; and (2) the relationship between reaction *P–T* and the major- and trace-element variability of the melt products. To address these aspects, we reacted basaltic glasses with orthopyroxenite (orthopyroxenite is one of most important pyroxenite) at 1300–1450 °C and 3.0–4.5 GPa. The experimental results enabled us to investigate the effects of basalt–pyroxenite reaction on the chemical composition of OIBs during their generation and evolution. The results reveal the causes of variations in the major- and trace-element compositions of OIBs and clarify the mechanisms by which OIBs evolve in the mantle.

2. Experimental and analytical methods

2.1. Starting materials

Basalt and orthopyroxene (Opx) were used as the starting materials, for which the major- and trace-element compositions are provided in Table 1. The basalt, DG-3, which was collected from Duge, Guizhou, China, is a typical Emeishan flood basalt and might have been generated within a typical mantle plume (Xu et al., 2001, 2004; Xiao et al., 2004). This basalt is a fresh greyish-green tholeiite, with amygdaloidal structure, and contains ~15 vol% plagioclase phenocryst and ~10 vol% clinopyroxene (Cpx) phenocryst. Its chemical composition is similar to that of OIB because similar processes generate flood basalts and OIBs. The aim of the experiment was to understand the major- and trace-element variations caused by basalt–pyroxenite reaction, so basalt compositionally similar to the average composition of Hawaiian OIBs was chosen. The composition of the reacted melts was then compared with the composition of OIBs to isolate the effects of melt–pyroxenite reaction. The major-element composition of DG-3 is similar to the average composition of Hawaiian OIBs, even there are some deviation on the TiO_2 and K_2O and MgO concentration (The effect of this deviation will be discussed in section 4.3). The concentration of trace elements in DG-3 is within an order of magnitude of the average trace-element concentrations in Hawaii OIBs, so DG-3 was considered to be an acceptable proxy for OIBs in these experiments. The basalt was crushed into chips, ground manually to powder in an agate mortar, melted in a crucible at 1500 °C and 1 atm for 1 h in air, and quenched. This cycle was repeated three times to produce a uniform glass that was examined with a scanning electron microscope. The basaltic glass was ground to a ~10 μm powder. The pyroxenite component of the experiment was provided by Opx grains (0.3–0.5 mm) separated from a lherzolite xenolith (No. DMP-01), collected

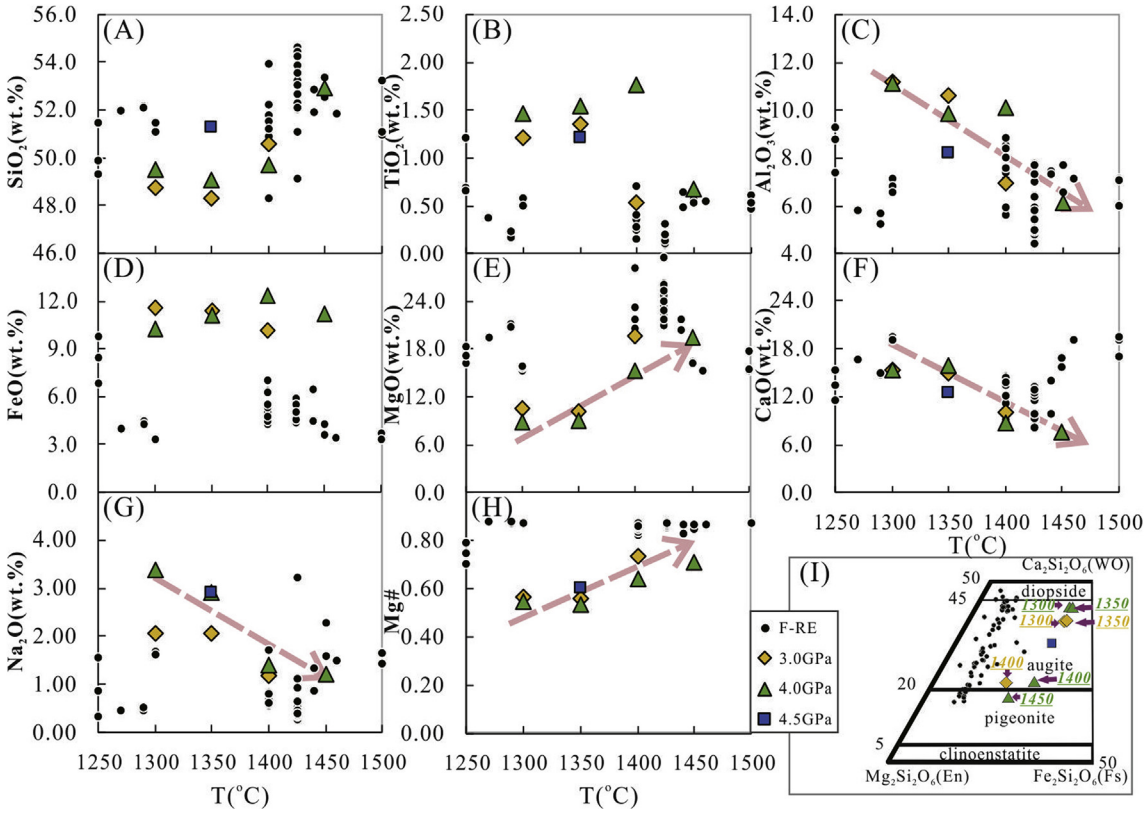

Fig. 5. Plots of major-element oxide concentrations and Mg# of newly grown Cpx in experimental products. F-RE: Cpx in basalt–peridotite experiments at 1250–1500 °C (Yaxley and Green, 1998; Lambart et al., 2009, 2012; Wang et al., 2010, 2013; Mallik and Dasgupta, 2012; Gao et al., 2017). 3.0 GPa, 4.0 GPa, 4.5 GPa: results from runs in this study at 3.0 GPa, 4.0 GPa, and 4.5 GPa, respectively. The schematic pyroxene classification diagram is from Morimoto (1988). Arrows mark the trends in concentrations and Mg# with increasing reaction temperature. Al_2O_3 and CaO content of Cpx decrease with increasing run temperature while the MgO and Mg# show crosscurrents. Compared with Cpxs in existing experiments (Yaxley and Green, 1998; Lambart et al., 2009, 2012; Wang et al., 2010, 2013; Mallik and Dasgupta, 2012; Gao et al., 2017), our Cpx enriched in TiO_2 and FeO, and depleted in SiO_2, MgO, and CaO.

from the Cainozoic Hannuoba basalt. This fresh lherzolite has a typical protogranular texture, and the forsterite and enstatite mole fractions of Ol and Opx, respectively, are up to 0.9, indicating that the lherzolite is a typical mantle rock and that the separated Opx is an acceptable substitute for mantle orthopyroxenite. Cpx may also exsit in mantle orthopyroxenites, while our preliminary experiment and existing studies (Shaw et al., 1998; Van Den Bleeken et al., 2011) all confirm the Cpx is one of newly growing minerals in basalt-pyroxenite reaction, and Cpx is probably inert during this reaction. Then we could use Opx only as a simplification of mantle orthopyroxenites, which makes the trace element analysis of experimental products feasible on LA-ICPMS. The prepared basaltic glass and Opx grains were cleaned ultrasonically and dried at 105 °C in an oven for more than 48 h to remove the adsorbed water, and stored in a drying box before use.

2.2. Experimental techniques

The experiments were conducted on a DS-3600 six-anvil apparatus at the Key Laboratory for High-Temperature and High-Pressure Study of Earth's Interior at the Institute of Geochemistry of the Chinese Academy of Sciences, Guiyang, China. The procedures were similar to those described by Wang and Tang (2013). The two starting materials were weighed in appropriate proportions (Table 2) and loaded in layers into graphite-lined platinum capsules to minimise Fe loss (Fig. 2). The capsules were covered with an Al_2O_3 sleeve, placed in the centre of a graphite heater, and the top of the assembly was filled with a pyrophyllite cylinder that had been fired at 800 °C. The graphite heating tube was then placed into a 32 mm pyrophyllite cube that had been fired at 800 °C (Fig. 2).

The temperature was measured and controlled via $PtRh_6$–$PtRh_{30}$ thermocouples with an accuracy of ±5 °C. The experimental pressure was determined by metal phase transformations using the high-purity bismuth phase transition pressure at room temperature and the gold melting pressure at 0.6–6.0 GPa (Fu and Zhu, 1986), and the KCl melting curve (Tingle et al., 1993). The two independent checks of pressure were in good agreement, and the uncertainty on pressure during runs was ±0.1 GPa, based on the variation of push-cylinder pressure. According to assessment of similar experiment using graphite-lined platinum capsules (Corgne et al., 2018), the oxygen fugacity within the experiment was between CCO and FMQ, which is similar to that of the mantle in the region of interest. During each run, the pressure was raised to the desired value; then, the temperature was increased in three steps (500 °C, 1000 °C, and final temperature) to the desired value. Pressure and temperature were maintained at the desired values for the duration of the experiment. The sample was quenched to <80 °C in 90 s by turning the power off and decompressing the charge. The products of each pre-synthesis run were removed carefully from the capsule, mounted in epoxy, and polished for inspection and electron microprobe analysis.

2.3. Analytical procedures

Chemical compositions of the basaltic glasses were determined at the State Key Laboratory of Ore Deposit Geochemistry of the Institute of Geochemistry, Chinese Academy of Sciences, Guiyang, China. Major elements were analysed using an Axios (PW4400) X-ray fluorescence spectrometer, and trace elements were analysed by inductively coupled plasma–mass spectrometry (ICP-MS) following the analytical procedure of Qi et al. (2000). Backscattered electron (BSE) images and the major-element concentrations of the run products were acquired using a JEOL JXA-8100 electron microprobe at the State Key Laboratory of

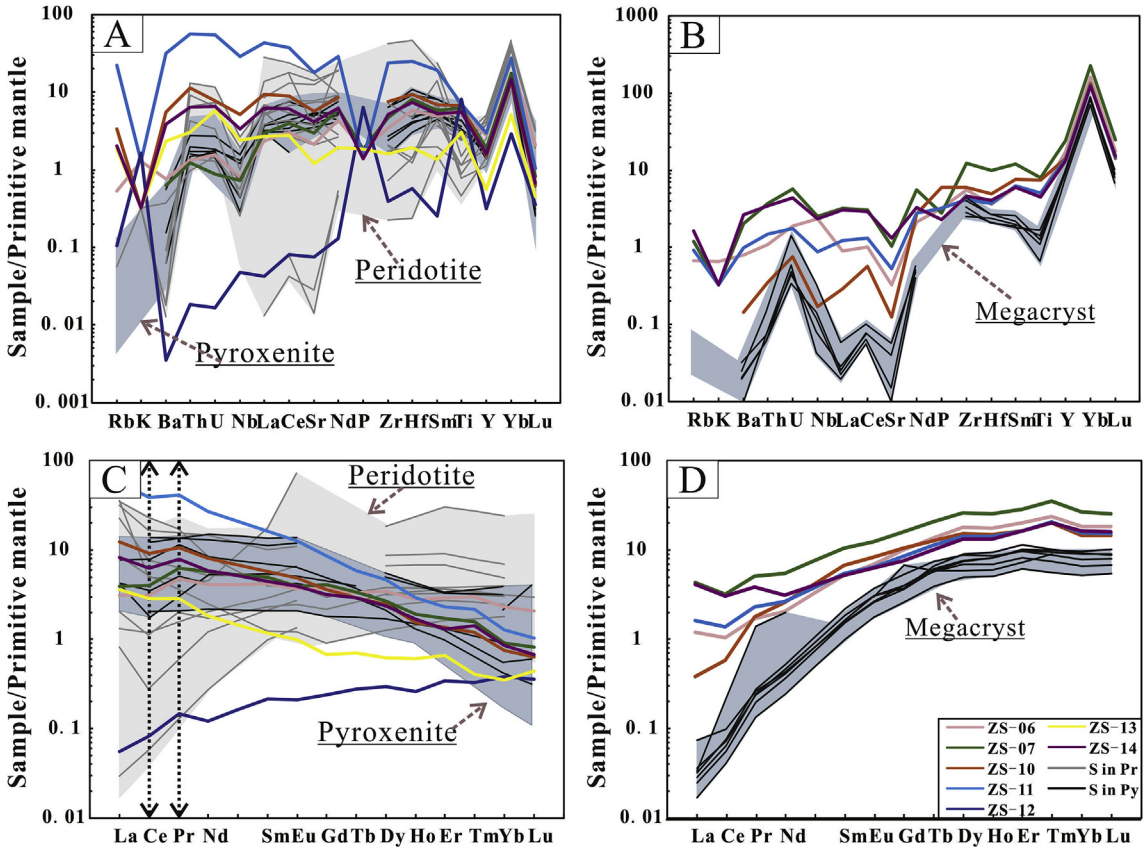

Fig. 6. Primitive-mantle-normalised spidergram and rare-earth-element patterns for natural and experimental Cpx (A, C) and Grt (B, D). The natural Cpx and Grt are from mantle xenoliths collected in Hawaii. ZS-06–ZS-14: newly grown Cpx and Grt, this study. S in Pr: representative Cpx in peridotite (dunite, harzburgite, and lherzolite). The range of variation of peridotites is shown by light-grey shading. S in Py: representative Cpx and Grt in pyroxenite (clinopyroxenite and megacrysts). Their range of variation is shown by light-blue–grey shading. Data from Cpx and Grt in Hawaiian mantle xenoliths are from the GEOROC database. The primitive-mantle and chondrite data used for normalisation are from Sun and Mcdonough (1989). Cpx in our runs (ZS-06, ZS-07, ZS-10 and ZS-14) match the ones in pyroxenite mantle xenoliths on primitive-mantle-normalised spidergram and rare-earth-element patterns diagram, indicating they may generate in similar process.

Isotope Geochemistry, Guangzhou Institute of Geochemistry, Chinese Academy of Sciences, Guangzhou, China. Analysis of the minerals and glass used a 1–5 μm focused beam, 15 kV accelerating voltage, and a 10 nA beam current, and followed the analytical method of Huang et al. (2007). Pure oxide standards were used for NiO and Cr_2O_3, and silicate minerals with compositions similar to those in the analysed samples were used as standards for the other major elements. Trace-element concentrations within the reacted melts were measured by laser ablation ICP-MS using a GeoLasPro laser ablation system and an Agilent 7700x ICP-MS instrument at the Sample Solution Analytical Technology Company, Wuhan, China. Details of the analytical procedures are reported by Liu et al. (2008) and the results of standard material are listed in Supplementary (Standard of trace element).

3. Results

3.1. Reaction assemblages

The reaction between the basaltic melt and Opx grains produced three distinct zones: residual Opx, reaction rims, and a melt pool (Fig. 3). The residual Opx grains are homogeneous. Backscattered electron (BSE) photomicrographs show some grey-level differences between Opx grains (Fig. 3A), but their major- and trace-element compositions are the same within the uncertainties of analysis. Reaction rims separate Opx grains from the residual melts. The reaction rims in runs at ≤1350 °C consist of newly grown Cpx and garnet (Grt), whereas the rims in runs at >1350 °C consist of Cpx only. The width of the reaction rims is a function of the *P–T* conditions and the relative positions of the Opx grains and melts. The width of the reaction rims in the 3.0 GPa runs is 50–150 μm in runs ZS-06 (1300 °C) and ZS-07 (1350 °C), and 20–60 μm in run ZS-08 (1400 °C). The width of the reaction rims in the 4.0 GPa experiments is > 700 μm in runs ZS-10/ZS-21 (1300 °C) and ZS-11 (1350 °C) (Fig. 3B and C), 50–200 μm in ZS-12 (1400 °C), and 3060 μm in ZS-13 (1450 °C). Reaction rims in run ZS-14 (4.5 GPa and 1350 °C) are 150–200 μm. Newly grown Cpx in the reaction rims formed banded or granular textures. Banded Cpx divided the melts from the residual Opx and formed in all runs. Granular Cpx occurred in mixtures with Grt crystals in the reaction rims that formed in runs ZS-07, ZS-10, ZS-11, ZS-14 and ZS-21 (Fig. 3B and C). Grt crystals in the reaction rims are euhedral to subhedral, and grew in pools of melt between Opx grains (Fig. 3A) or with granular Cpx (Fig. 3B and C). Glass formed from the quenched melts is present in all runs except ZS-10, where the melt quenched to Cpx (Fig. 3B). Glasses in the run products are homogeneous and clear, and melt quench products commonly occur close to the reaction rims (Fig. 3D; ZS-12). Our results differ from those of basalt–peridotite experiments (Yaxley and Green, 1998; Van Den Bleeken et al., 2011; Gao et al., 2017), where the rims are Opx ± Grt (>2.0 GPa) or Ol ± Opx ± Cpx (<2.0 GPa). Our results also differ from those of basalt–Opx experiments at 1 atm (Shaw et al., 1998); Ol occurs in the reaction rims at 1 atm, but not at the higher pressures of our experiments. Furthermore, Grt did not form in their low-pressure experiments, but formed in our experiments at ≤1350 °C.

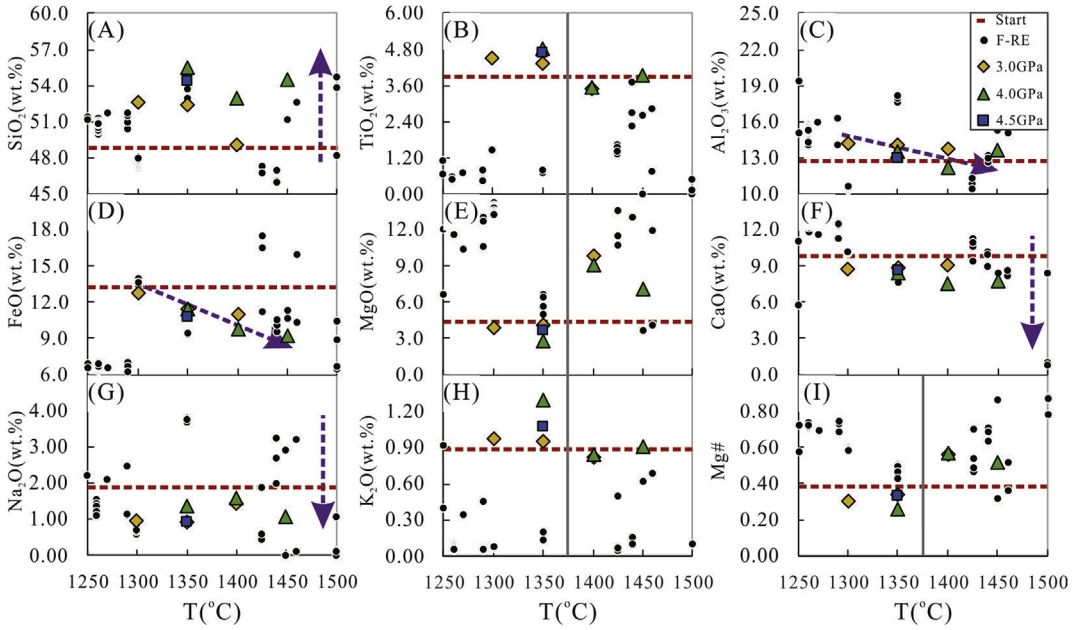

Fig. 7. Plots of major-element oxide concentrations and the Mg# of residual melts in experimental products. Start: composition of starting melt. F-RE: residual melts in basalt–peridotite experiments at 1250–1500 °C (Lambart et al., 2009, 2012; Wang et al., 2010, 2013, 2016; Van Den Bleeken et al., 2011; Gao et al., 2017). 3.0 GPa, 4.0 GPa, 4.5 GPa: results from runs in this study at 3.0 GPa, 4.0 GPa, and 4.5 GPa, respectively. Arrows indicate the trends in concentrations and Mg# with increasing reaction temperature. Reacted melt elevate their SiO_2 content during the reaction, which is very different from residual melts in basalt–peridotite experiments (Lambart et al., 2009, 2012; Wang et al., 2010, 2013, 2016; Van Den Bleeken et al., 2011; Gao et al., 2017), this may be caused by the high SiO_2 concentration of Opx relative to that of peridotite.

3.2. Chemical compositions of run products

The reaction between basaltic melt and Opx grains altered the chemical composition of the phases (Supplementary Table S1). Minerals and melts in the run products are homogeneous with respect to major and trace elements, with variation of <2% relative for major elements and <10% relative for trace elements.

The major-element composition of residual Opx is similar before and after reaction (Fig. 4). This result is consistent with measurements of the compositions of residual Opx in basalt–peridotite experiments (Yaxley and Green, 1998; Mallik and Dasgupta, 2012; Gao et al., 2017) but different from those for Opx in basalt–peridotite experiments where Opx dissolution occurred (Wang et al., 2013, 2016). Starting and reacted Opxs are classified as enstatite, similar to those in other experiments (Fig. 4H). With respect to trace elements, the unreacted Opx was enriched in Sc, V, Cr, Co, Ni, Zn, and Ga (>3 ppm). Concentrations of these trace elements in the residual Opxs were almost unchanged by the experiments, except for run ZS-08 (3.0 GPa and 1400 °C), where the V, Cr, Co, Ni, Zn, and Ga concentrations of reacted Opx are much higher than those of the starting Opx. The Sc concentration of Opx in run ZS-08 decreased to 0.35 ppm, which is much lower than that of the starting Opx. The Cr/V value of residual Opx in most of the runs is 19.5–21.8, which is close to the value of 21 measured in the starting Opx. However, Cr/V is 146 in the residual Opx of run ZS-08. The value of Ni/Co is 12.8–14.3, which is close to the value of 14.0 measured in the starting Opx. These trends of the trace-element concentrations of residual Opx are different from those described by Rapp et al. (2010); the trace-element content of Opx changed drastically during their experiments, with trends similar to those observed in our run ZS-08. The reason for these differences is discussed in section 4.1.

Concentrations of Al_2O_3 and CaO in newly grown Cpx decrease with increasing run temperature (Fig. 5), whereas the MgO concentration and Mg# [= molar MgO/(Mg + ΣFeO)] show crosscurrents. The newly grown Cpxs in our experiments have higher TiO_2 and FeO concentrations, lower SiO_2, MgO, and CaO concentrations, and lower Mg# compared with Cpxs in existing basalt–peridotite experiments (Yaxley and Green, 1998; Lambart et al., 2009, 2012; Wang et al., 2010, 2013; Mallik and Dasgupta, 2012; Gao et al., 2017) (Fig. 5). The newly grown Cpxs in our runs are almost all augites (Fig. 5I), except in run ZS-13, where the newly grown Cpx is pigeonite. With increasing run temperature, the proportion of enstatite in the newly grown Cpx in reaction rims increases and the proportions of $Ca_2Si_2O_6$ (Wo) and $Fe_2Si_2O_6$ (Fs) decrease. The newly grown Cpxs in our experimental products are enriched in Fs compared with those grown in basalt–peridotite reactions, which may due to lower MgO content of starting basalt. With respect to trace elements, newly grown Cpx contains Sc, V, Cr, Co, Ni, Zn, Ga, Sr, Zr, and Ba, and rare-earth elements (REEs). Their total REE contents (ΣREE, not including Y) range from 1.4 to 167.5 ppm, with most of the runs containing ~30 ppm. δEu [= $Eu_N/0.5(Sm_N + Gd_N)$] values are 0.8–1.1, and δCe [= $Ce_N/0.5(La_N + Pr_N)$] values range from 1.0 to 1.15. The newly grown Cpx shows negative Y anomalies and positive Yb anomalies on a primitive-mantle-normalised spidergram (Fig. 6A), and REE contents decrease towards the heavy REEs (HREEs), with the exception of run ZS-12. The value of Cr/V in Cpx is 0.38–5.57, and the value of Ni/Co is 1.76–8.12.

Grt also occurs as a newly grown mineral in reaction rims, SiO_2 and Al_2O_3 concentrations of Grt are relatively consistent. FeO and CaO concentrations of Grt in ZS-07 (3.0 GPa, 1350 °C) are higher than those in ZS-06 (3.0 GPa, 1300 °C), and the MgO concentration is lower. In runs at 4.0 GPa, FeO and CaO concentrations of Grt decrease further, whereas the MgO concentration of Grt increases with increasing temperature (Supplementary Table S1). The Grt is enriched in Sc, V, Cr, Co, Ni, Zn, Ga, Sr, Zr, Ba, and HREEs. ΣREE contents, not including Y, range from 48.5 to 90.1 ppm, δEu values are 0.9–0.97, and δCe values are 0.54–0.76. The newly grown Grts show a negative Sr anomaly and a positive Yb anomaly on a primitive-mantle-normalised spidergram (Fig. 6B), and the normalised REE concentrations increase towards the HREEs (Fig. 6D). The value of Cr/V in Grt is 0.61–2.08 and Ni/Co is 0.46–1.07.

The SiO_2 concentration of the melt phase increased after reaction (Fig. 7A), and CaO and Na_2O concentrations decreased (Fig. 7F and G). Al_2O_3 and FeO concentrations show a linear decrease with increasing reaction temperature (Fig. 7C and D). The runs at ≤1350 °C show

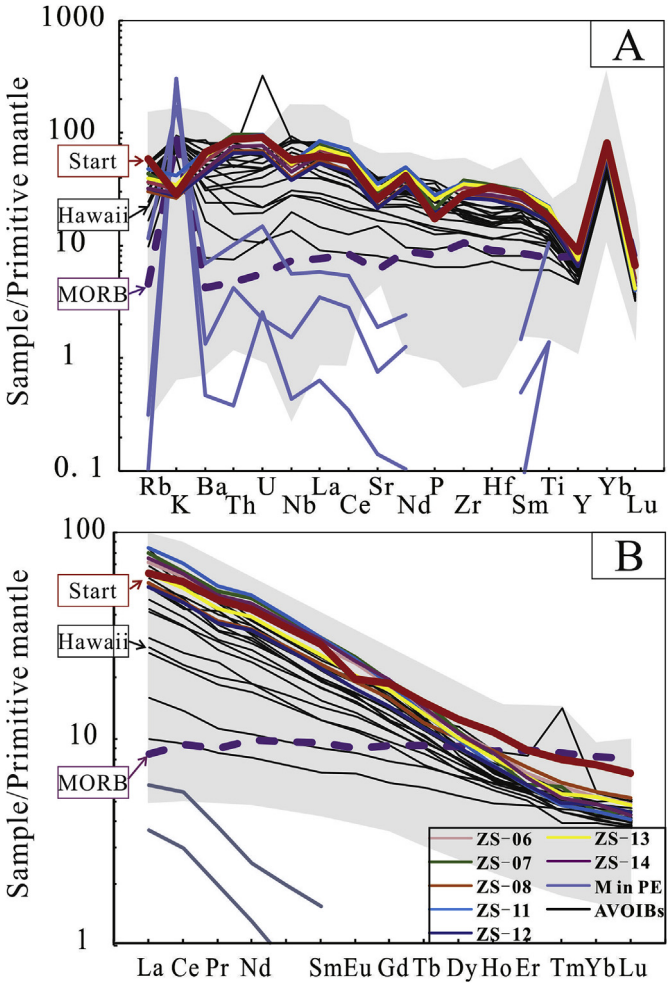

Fig. 8. Primitive-mantle-normalised spidergram and rare-earth-element patterns for the residual experimental melts and OIBs. ZS-06–ZS-14: residual melts, this study. M in PE: residual melts, peridotite–basalt experiments (Tominaga et al., 2009). AVOIBs: average trace-element composition of 18 typical OIBs, with data for these OIBs and MORB from Huang and Zheng (2017). The range of variation of Hawaiian OIBs is shown by light-grey shading. Data for the Hawaiian OIBs are from the GEOROC database, our results match field observation better than result from peridotite–basalt experiment.

different trends for TiO_2, MgO, K_2O, and Mg# compared with those at ≥1400 °C (Fig. 7B, E, H, and I). In runs at ≤1350 °C, TiO_2 and K_2O concentrations of the product glass are higher than those in the initial glass, and the MgO concentration and Mg# are lower than in the initial glass. In contrast, at runs at ≥1400 °C, TiO_2 and K_2O concentrations of the product glass are lower than those of the initial glass, and MgO concentration and Mg# are higher than in the initial glass. The residual melts in this study are enriched in SiO_2, TiO_2, and K_2O relative to the residual melts in basalt–peridotite experiments (Lambart et al., 2009, 2012; Wang et al., 2010, 2013, 2016; Van Den Bleeken et al., 2011; Gao et al., 2017) (Fig. 7A, B, and H). The high SiO_2 concentration of the residual melt in our experiments might be attributable to the high SiO_2 concentration of Opx relative to that of peridotite, and the high TiO_2 and K_2O concentrations might reflect their high concentrations in the starting material. The residual melts are enriched in trace elements such as Sc, V, Cr, Co, Ni, Zn, Ga, Rb, Sr, Y, Zr, Nb, and Ba and light REEs (LREEs). ΣREE contents (not including Y) range from 215 to 308 ppm, the value of δEu is 0.95–1.01, and the value of δCe is 0.99–1.02. The residual melts show a negative Y anomaly and a positive Yb anomaly on a primitive-mantle normalised spidergram (Fig. 8A), and the REE patterns slope down towards the HREEs (Fig. 8B).

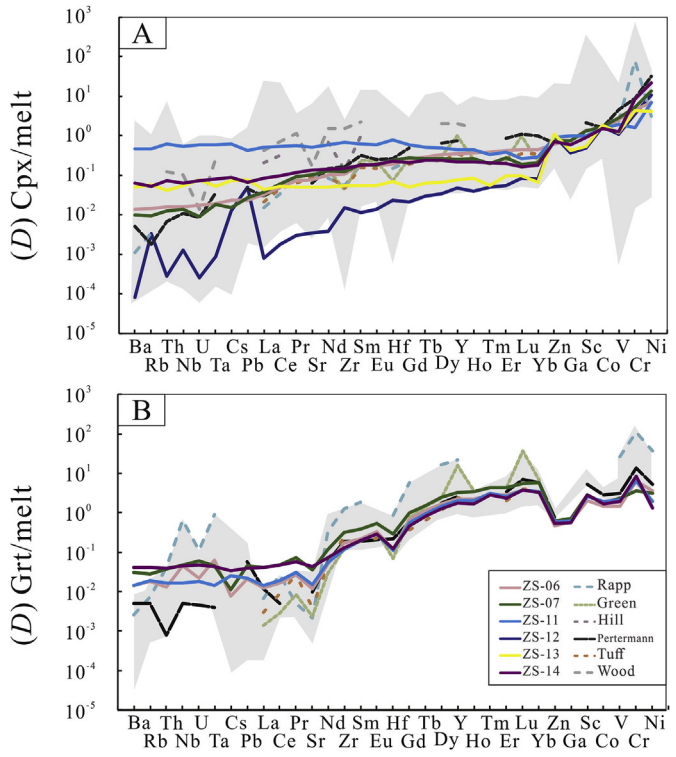

Fig. 9. Calculated trace-element mineral–melt *D* values. ZS-06–ZS-14: experimental data, this study. The range of variation in *D* values is shown by light-grey shading. Data for $D_{Cpx-melt}$ are from the supplementary data of Bédard (2014), and data for $D_{Cpx/melt}$ are summarised from existing experimental data (Salters and Longhi, 1999; Green et al., 2000; Klemme et al., 2002; Tuff and Gibson, 2007; Rapp et al., 2010; Pertermann et al., 2004). Rapp, Green, Hill, Pertermann, Tuff and Wood refer to representative values from Rapp et al. (2010), Green et al. (2000), Hill et al. (2011), Pertermann et al. (2004), Tuff and Gibson (2007), and Wood and Trigila (2001), respectively.

4. Discussion

4.1. Reaction mechanism and equilibrium

The reaction between basaltic melt and Opx produced reaction rims that separate the residual melt from the Opx grains. The minerals and melts are homogeneous with respect to their major- and trace-element compositions, and the major-element composition of Opx grains did not change during the reaction (Fig. 4; Supplementary Table S1). Wang et al. (2019) summarised the three possible types of reaction between melt and rocks: dissolution reactions, completely equilibrated reactions, and locally equilibrated reactions. Dissolution usually occurs within high-temperature, short-duration (<8 h) layered experiments (Liang et al., 1996; Morgan and Liang, 2005; Wang et al., 2016), and these reactions induce pronounced differences in the major-element compositions of minerals and melts as a function of the distance from melt–mineral contacts. The glass and mineral products of our experiments did not show such differences in major-element concentrations, so any dissolution is likely to have been completed prior to the end of our experiments. Completely equilibrated reactions are usually found in hydrous layered experiments (Rapp et al., 1999, 2010) or experiments with mixed components (Johnston and Wyllie, 1989; Mallik and Dasgupta, 2012). Residual minerals are not normally found in completely equilibrated experiments because all of the minerals are newly grown during the equilibrating reactions. In our experiments, the Opx is clearly residual, so complete equilibration did not occur. Our results are consistent with those described for local equilibrium reactions (Yaxley and Green, 1998; Wang et al., 2010, 2019; Wang and Tang, 2013). For

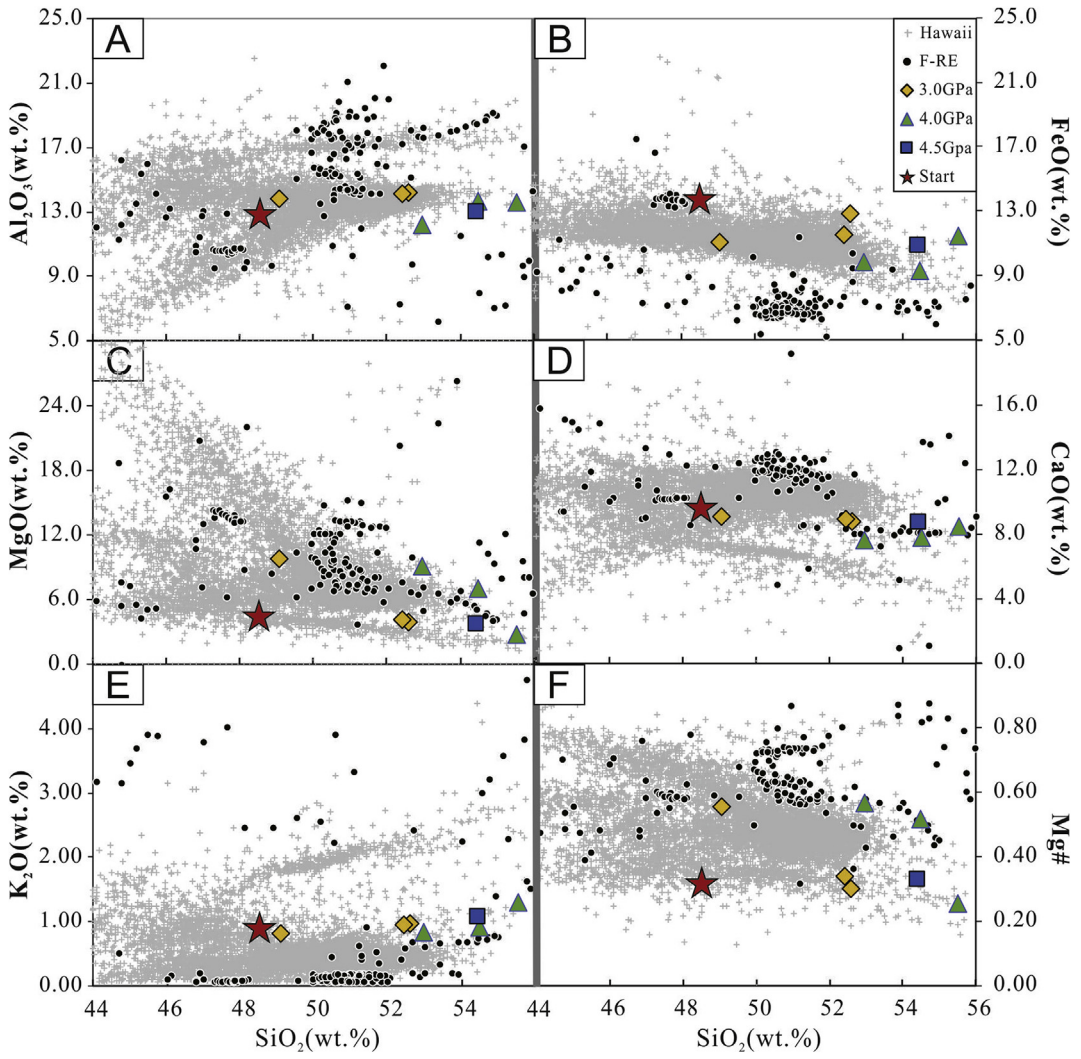

Fig. 10. Harker diagrams for reacted melt in the experimental products and natural Hawaiian basalts. Data for the Hawaiian basalts are from the GEOROC database. F-RE: residual melts in basalt–peridotite experiments (Yaxley and Green, 1998; Lambart et al., 2009, 2012; Wang et al., 2010, 2013, 2016; Van Den Bleeken et al., 2011). 3.0 GPa, 4.0 GPa, and 4.5 GPa refer to residual melts from runs in this study at 3.0 GPa, 4.0 GPa, and 4.5 GPa, respectively. Start: composition of starting melt. Melts' major element variation in our experiment cover the range of high SiO_2 basalt from Hawaii except on K_2O vs. SiO_2 (K_2O content is mainly controlled by the starting composition), indicating that reaction between basalt and Opx might contribute to the generation of Hawaiian high-SiO_2 OIBs and account for their chemical variability.

example, there are obvious reaction rims in our experiments that separate the residual minerals from the melt. Then we need to consider the equilibrium between newly born minerals (Cpx and Grt) and residual melts, we believed the equilibrium between them are achieved, the reasons are following: (1) Experiment at similar run conditions ($T \geq$ 1350 °C) achieved equilibrium after ~48 h run duration, such as Yaxley and Green (1998) and Wang et al. (2010), so our runs at ≥1350 °C should close to or achieved equilibrium; (2) The garnet–pyroxene Fe^{2+}–Mg geothermometer was used to examine the reaction equilibrium according to Ravna (2000), the calculation result of ZS-10 is 1285 °C, very close to the design temperature (1300 °C). As this temperature is the lowest desired one in our runs, other runs at high temperature should approach equilibrium between newly born minerals (Cpx and Grt) and residual melts; (3) A protraction run (ZS-21, 60 h) was conduct to check the local equilibrium of ZS-10, as this run has no residual melt in experiment product. In order to get residual melt in run product, the ZS-21 has lower Opx/glass ratio (1:1) than ZS-10 (2:1), but the phase assemblage of them are almost the same except there are few residual melt in ZS-21 (Table 2). The major element composition of minerals in these two run products is also very similar: (1) Opx in ZS-21 has the same major element composition as the one in ZS-10; and (2) the newly grown minerals Cpx and Grt in ZS-21 are close to these in ZS-10 in their major element composition. This result indicates that the ZS-10 is close to equilibrium between newly grown minerals (Cpx and Grt) and residual melts (Supplementary Table S1). And this equilibration might have involved the following two steps: (1) Opx grains dissolved in the initial melt, and the chemical composition of melt changed to Melt 1, as described by Reaction (I); and (2) dissolution ceased when Cpx crystals began to precipitate from Melt 1. The newly formed Cpx was banded, and it separated the Opx grains from Melt 1. In runs at ≤ 1350 °C, Cpx and Grt crystallised sequentially or simultaneously, whereas in runs at ≥ 1400 °C, granular Cpx crystallised, and caused Melt 1 to change its chemical composition to Melt (residual), as described by Reaction (II). This local equilibrium hypothesis explains most of the features of the trace-element distribution, except for the trace-element concentrations of the Opx grains of run ZS-08. The V, Cr, Co, and Ni concentrations of the Opx grains in run ZS-08 are many times higher than those of the Opx grains in other runs and the starting material. This indicates that the Opx grains might have concentrated the V, Cr, Co, and Ni before the Opx dissolved into Melt 1. This process would be slow if the Opx grains were solid but rapid within a

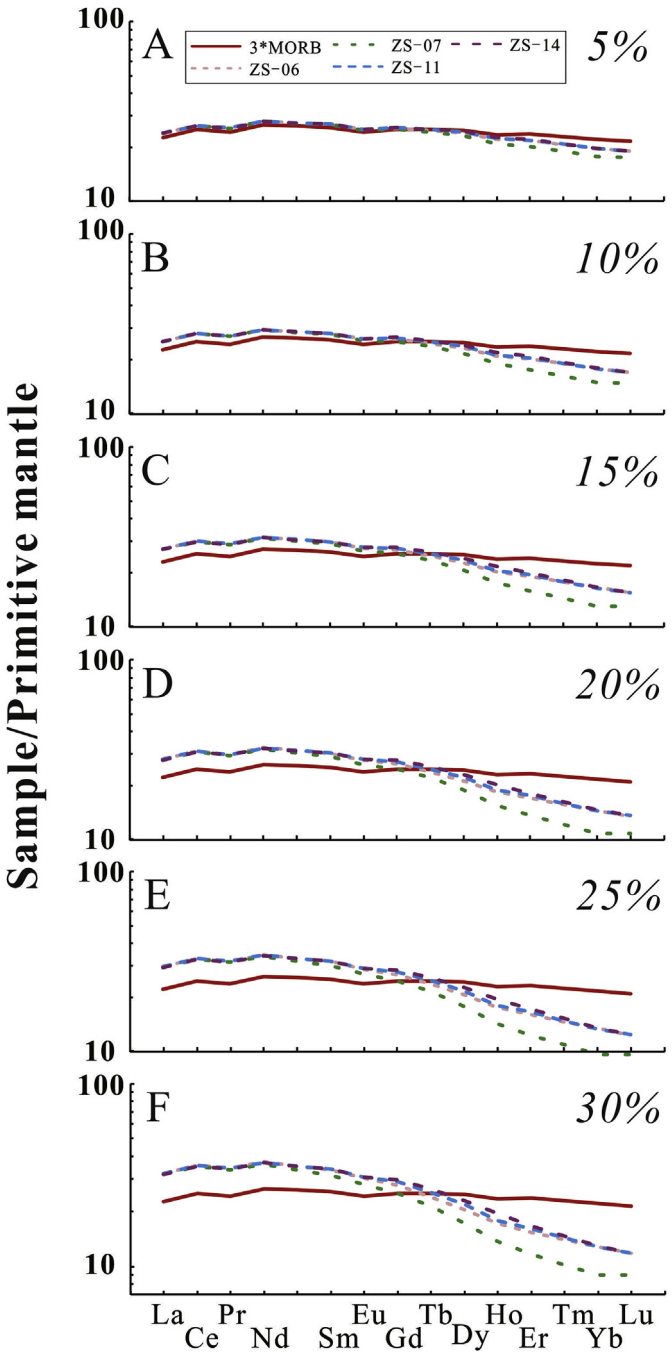

Fig. 11. Calculated primitive-mantle-normalised REE patterns for residual melt after crystallisation of 5–30 wt.% Grt. For clarity, a melt with REE contents three times higher than MORB was chosen as the starting melt. Data for starting melt are from Huang and Zheng (2017). ZS-06–ZS-14: results calculated from values of $D_{Grt–melt}$ listed in Supplementary Table S2. The weight percentage of garnet crystallised (X) is shown in the top-right corner of each diagram, and the corresponding weight percentage of melt is 100 − X. According to this calculation, a starting melt with a flat REE pattern could get a rightleaning REE patterns after crystallisation and removal of 15–20 wt.% Grt.

liquid. Therefore, the Opx solidus might be close to 1400 °C at 3.0 GPa (Pertermann and Hirschmann, 2003; Anderson, 2005), and the trace elements might have concentrated during Opx dissolution. This result indicates that the trace-element content of Opx can change dramatically when Opx is close to, or at, its solidus.

$$\text{Opx} + \text{Melt(start)} \rightarrow \text{Melt 1} \quad (1)$$

$$\text{Melt 1} \rightarrow \text{Opx(r)} \pm \text{Grt(r)} + \text{Melt(residual)}\ [\text{(r): mineral in reaction rim}] \quad (2)$$

4.2. Mineral–melt distribution coefficients (D values)

According to the reaction mechanism proposed above, the two newly grown minerals, Cpx and Grt, crystallised from Melt 1, and equilibrium would have been maintained with the residual melt. Mineral–melt distribution coefficients were calculated on the basis of this assumption (Supplementary Table S2). The validity of these *D* values depends on the analytical detection limits of the incompatible elements in minerals (Rapp et al., 2010), and *D* values might also be a function of pressure, temperature, and mineral compositions (Wim et al., 1999; Wood and Trigila, 2001; Westrenen and Draper, 2007; Bédard, 2014). Our results provide *D* values for Cpx–basalt and Grt–basalt in mantle environments and constitute a valuable resource that enables interpretation of the relationship between melt–rock reaction and the compositional variation of OIBs.

The values of $D_{Cpx–melt}$ calculated from our results are consistent with the database of Bédard (2014) (Fig. 9A). The most incompatible elements in Cpx in our study are Ba, Rb, Th, U, Nb, Ta, and Cs, and the $D_{Cpx–melt}$ values of these elements were affected by the temperature and pressure of reactions. For these elements, $D_{Cpx–melt}$ values at 4.0 and 4.5 GPa are higher than those at 3.0 GPa, indicating that the compatibility of these elements increases with increasing pressure. The effects of temperature on the $D_{Cpx–melt}$ values of Ba, Rb, Th, U, Nb, Ta, and Cs are barely noticeable at 3.0 GPa. $D_{Cpx–melt}$ values of these elements decrease as run temperature increases, consistent with the results of Bédard (2014). Strontium, Zr, and REEs are also incompatible in Cpx; $D_{Cpx–melt}$ values of these trace elements are effectively identical in the runs at 4.0 and 4.5 GPa. However, at 3.0 GPa, $D_{Cpx–melt}$ values of these trace elements are higher than those of Ba, Rb, Th, U, Nb, Ta, and Cs. Zinc, Ga, Sc, Co, Cr, and Ni are compatible elements in Cpx, and changes to the reaction pressure and temperature had little effect on the partition coefficients. Our results are similar to those of Pertermann et al. (2004), except for HREEs. The results of Green et al. (2000) and show some peaks at Y and Lu in REE curves, but the range of concentrations in their experiments is consistent with the variation in the concentrations presented here.

There is little change in $D_{Grt–melt}$ values with changes in *P* and *T*, in contrast to the observed changes in $D_{Cpx–melt}$ (Fig. 9B). Barium, Rb, Th, U, Nb, Ta, Cs, Zn, Ga, and LREEs are incompatible in garnet, whereas HREEs, Sc, Co, Cr, and Ni are compatible. There are marked negative Sr and Hf anomalies, and a positive Cr anomaly; these anomalies are consistent with those noted in previous studies (Green et al., 2000; Wood and Trigila, 2001; Tuff and Gibson, 2007; Xiong and Han, 2007) and the calculated $D_{Grt–melt}$ values of compatible elements are similar to those of Pertermann et al. (2004).

4.3. Effects of the melt–pyroxenite reaction on the evolution of ocean island basalts in the mantle

Some researchers have noted that reactions between basaltic melt and peridotite and/or pyroxenite play an important role in the generation of chemical variation in high-SiO_2 OIBs (Wagner and Grove, 1998; Stolper et al., 2004; Putirka et al., 2011), but until now there has been no experimental petrological evidence to support this hypothesis. As stated by Jackson et al. (2012), explanations of OIB chemistry that involve interactions of melt with peridotite or pyroxenite must account for two features of OIB: (1) Ol precipitated during melt–rock reaction would produce a positive trend in SiO_2 vs. CaO/Al_2O_3 space; and (2) the trace-element signature of residual Grt is observed in OIBs. In the following, we discuss whether OIBs might be generated by the melt–rock reactions we propose here, based on the results reported in this study.

Our experimental results indicate that basalt–Opx reaction produces Cpx or Cpx + Grt but not Ol. This result differs from the predictions of Kelemen et al. (1992); the reason for the lack of olivine in our experiments

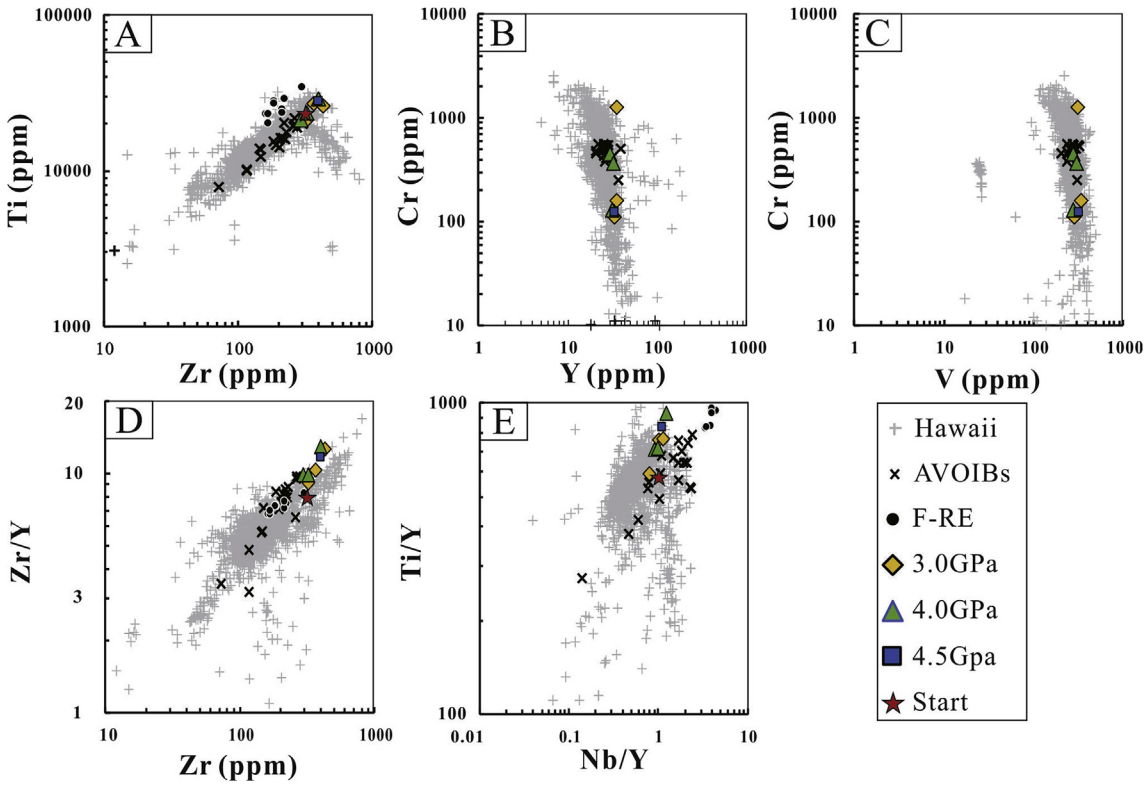

Fig. 12. Diagrams of (A) Ti vs. Zr, (B) Cr vs. Y, (C) Cr vs. V, (D) Zr/Y vs. Zr, and (E) Ti/Y vs. Nb/Y. Hawaii: Hawaiian basalt, data are from the GEOROC database. AVOIBs: average trace-element composition of 18 typical OIBs, with data for these OIBs from Huang and Zheng (2017). F-RE: residual melts from basalt–peridotite experiments (Tominaga et al., 2009). 3.0 GPa, 4.0 GPa, 4.5 GPa refer to residual melts from runs in this study at 3.0 GPa, 4.0 GPa, and 4.5 GPa, respectively. Start: composition of starting melt. Our melts' trace elements variation range match well with OIB's on these classical absolute trace-element concentrations and conventional trace-element-ratio diagrams, indicating that the observed compositional variation of OIBs might reflect basalt–orthopyroxenite interactions.

might be the high pressures of reaction, based on a comparison of our results with those of Shaw et al. (1998). This result is consistent with the similar reactions between silicate melt and peridotite, Ol precipitates in low pressure reactions (1 atm–1.5 GPa) (Shaw and Dingwell, 2007; Sébastien et al., 2008; Van Den Bleeken et al., 2011; Lambart et al., 2012) and absents at high pressure reaction($\geq$2.0 GPa) (Yaxley and Green, 1998; Rapp et al., 1999; Tominaga et al., 2009; Wang et al., 2010; Mallik and Dasgupta, 2012; Gao et al., 2017), indicating that Ol is difficult to saturate in silicates at high pressure ($\geq$2.0 GPa). The mineral assemblage in our experimental products indicates that the residual rock in the mantle should be pyroxenite or garnet pyroxenite; these rocks are observed in mantle xenoliths from Hawaii (Garcia and Presti, 1987; Sen, 1988; Stracke et al., 2018). Primitive-mantle-normalised spidergrams and REE patterns for the Cpx in these pyroxenite mantle xenoliths match our experimental results with the data from Hawaiian peridotite xenoliths (Fig. 6A and C), indicating that the pyroxenite mantle xenoliths might be the product of reaction between basaltic melt and orthopyroxenite. The possible compositional variations caused by melt–Opx reaction were assessed using major-element Harker diagrams (Fig. 10), and the trends were compared with those observed in the Hawaiian OIBs. The composition of the residual melt differs considerably from that of the starting melt (Fig. 10), with residual melt compositions that cover almost the entire range of high-SiO_2 basalt compositions (SiO_2 concentration $\geq$ 48 wt.%). On SiO_2–Al_2O_3 (Fig. 10A) and SiO_2–FeO (Fig. 10B) diagrams, the residual melts produced at 3.0 GPa are closer to the natural melt compositions from Hawaii compared with the melts produced at 4.0 and 4.5 GPa. The residual melts produced at 3.0 and 4.0 GPa match the variation of the natural Hawaiian samples with respect to SiO_2–MgO (Fig. 10C) and SiO_2–Mg# (Fig. 10F). The CaO concentrations of the residual melts produced in this study are slightly less than those of most Hawaii OIBs (Fig. 10D), and the K_2O concentrations are slightly higher (Fig. 10E). Compared with residual melts produced by basalt–peridotite reaction, our residual melts match the Hawaii OIBs better in SiO_2–FeO space (Fig. 10B) and SiO_2–Mg# space (Fig. 10F). Then we also need to consider the effect of starting basalt, as our starting basaltic glass have a higher TiO_2 and K_2O content and lower MgO content than the average compositions of Hawaii OIBs. According to experiment result, potassium is incompatible element for Cpx and Grt, its content in residual melt depends on its starting concentrations. The behaviour of titanium is almost the same with potassium during the reaction, although the titanium could join in the newly grown Cpx and Grt, while their $D_{\text{mineral–melt}}$ values (the calculation of $D_{\text{mineral–melt}}$ values is based on the data in Supplementary Table S1) are about 0.15–0.50, so the titanium is also mainly existing in the residual melt as there is no independent titanium-rich mineral in our reaction products. The MgO content of residual melt is also affected by the staring basalt, and the residual melts at runs $\leq$ 1350 °C may have a higher MgO content if the MgO content of starting basalt is close to average compositions of Hawaii OIBs. After these amendments above, our residual melts will match Hawaiian high-SiO_2 basalts better than now if our starting basalt is more close to average compositions of Hawaii OIBs. This result also indicates that these OIBs might be residual melts produced by reaction between a basaltic melt and orthopyroxenite.

As mentioned above, OIBs show a trace-element signature attributable to residual Grt. Grt is a product of basalt–orthopyroxenite reaction in the runs at $\leq$1350 °C, so the residual melts of these runs should show the effects of Grt fractionation. The REE patterns of the residual melts in our experiments all slope downwards to the right, which might reflect the presence of residual garnet, or might be inherited from the starting basalt (Fig. 8B). To account for the influence of the starting melt on REE patterns, we calculated the REE pattern of a residual melt produced from a

starting melt with a flat REE pattern, using the values of $D_{Grt-melt}$ from our experiments (Fig. 11). The residual melt has an REE pattern that slopes down to the right after crystallisation and removal of 15–20 wt.% Grt. This Grt proportion was observed in the BSE photomicrographs of the 4.0 GPa run products (ZS-10 and ZS-11, Fig. 3B and C), indicating that basalt–orthopyroxenite reaction at ~130 km depth might produce residual melts with the trace-element signature of residual Grt. We also compared the residual melt with Hawaiian OIBs using absolute trace-element concentrations and conventional trace-element-ratio diagrams (Chen et al., 2017, and references therein) (Fig. 12). The residual melts produced in this study cover some of the range in variation shown by Hawaiian OIBs on Ti vs. Zr (Fig. 12A) and Zr/Y vs. Zr (Fig. 12D) diagrams, and most of the compositional range shown by Hawaiian OIBs on Cr vs. Y (Fig. 12B) and Cr vs. V (Fig. 12C) diagrams. On a Ti/Y vs. Nb/Y diagram (Fig. 12E), the residual melt compositions coincide with part of the compositional range of Hawaiian OIBs. Our results match the Hawaiian OIBs better than do those of basalt–peridotite experiments on Ti vs. Zr and Ti/Y vs. Nb/Y diagrams. These excellent matches indicate that the observed compositional variation of OIBs might reflect basalt–orthopyroxenite interactions.

5. Conclusions

Basaltic melt and Opx grains were reacted at 3.0–4.5 GPa and 1300–1450 °C to simulate the evolution of OIBs in response to basalt–orthopyroxenite reaction during the residence and transport of magma in the mantle. Our results were used to derive the following conclusions regarding trace-element mineral–melt distribution coefficients, basalt–orthopyroxenite reaction in the mantle, and the major- and trace-element evolution of OIB.

(1) Basaltic melt and Opx grains reached a locally equilibrated state during 48 h experiments at 3.0–4.5 GPa and 1300–1450 °C. The reaction process might have involved: (i) dissolution of Opx by the starting melt with concomitant variation in the melt composition and eventual Cpx saturation; and (ii) precipitation of new banded Cpx that spatially separates Opx from the melt and continued crystallisation of Cpx with or without Grt.
(2) The most incompatible elements in Cpx were Ba, Rb, Th, U, Nb, Ta, and Cs. The compatibility of these elements increased with increasing pressure. Zinc, Ga, Sc, Co, Cr, and Ni were compatible in Cpx, and there was no distinguishable effect of *P* and *T* on the compatibility of these elements. Barium, Rb, Th, U, Nb, Ta, Cs, Zn, Ga, and LREEs were incompatible in garnet, whereas HREEs, Sc, Co, Cr and Ni were compatible. The effect of *P* and *T* on the compatibility of trace elements in Grt was negligible.
(3) Basalt–Opx reaction induced precipitation of Cpx or Cpx + Grt; Ol was not observed. This indicates that the residual rock should be pyroxenite or garnet pyroxenite, consistent with field observations from Hawaii. The residual melts in our experimental products are enriched in SiO_2, and their major- and trace-element variations match those of natural samples from Hawaii, indicating that reaction between basaltic melt and pyroxenite might have contributed to the generation of chemical variation in Hawaiian high-SiO_2 OIBs.

Declaration of competing interest

The authors declare that they have no known competing financial interests or personal relationships that could have appeared to influence the work reported in this paper.

Acknowledgements

We sincerely thank the three anonymous reviewers for their helpful comments and suggestions on the manuscript. We also thank Prof. Jianguo Du for his invitation, Prof. Wenge Zhou for useful discussions, Prof. Chengming Zhu and Mr. Enzhao Cai for technical assistance in high-pressure apparatus operation, and Dr. Linli Chen for support and help in electron microprobe analysis. This work was financially supported by Natural Science Foundations of China (Grant Nos. 41502057 and 41472065), Foundations of Suzhou University (Nos. 2019ZD46, 2015jb01 and 2015jb07).

Appendix A. Supplementary data

Supplementary data to this article can be found online at https://doi.org/10.1016/j.gsf.2020.05.023.

References

Anderson, D.L., 2005. Large igneous provinces, delamination, and fertile mantle. Elements 1, 271–275.
Bédard, J.H., 2014. Parameterizations of calcic clinopyroxene: melt trace element partition coefficients. G-cubed 15, 303–336.
Borisova, A.Y., Bohrson, W.A., Grégoire, M., 2017. Origin of primitive ocean island basalts by crustal gabbro assimilation and multiple recharge of plume-derived melts. G-cubed 18, 2701–2716.
Borisova, A.Y., Nikogosian, I.K., Scoates, J.S., Weis, D., Damasceno, D., Shimizu, N., Touret, J.L.R., 2002. Melt, fluid and crystal inclusions in olivine phenocrysts from Kerguelen plume-derived picritic basalts: evidence for interaction with the Kerguelen Plateau lithosphere. Chem. Geol. 183, 195–220.
Caroff, M., Maury, R.C., Vidal, P., Guille, G., Dupuy, C., Cotten, J., Guillou, H., Gillot, P., 1995. Rapid temporal changes in ocean island basalt composition: evidence from an 800 m deep drill hole in Eiao Shield (Marquesas). J. Petrol. 36, 1333–1365.
Chen, W., Wang, J., Zhang, Q., Liu, Y., Li, M.A., Jiao, S., 2017. Data mining of ocean island basalt and ocean plateau basalt: geochemical characteristics and comparison with MORB. Acta Geol. Sin. 91 (11), 2443–2455 (in Chinese with English abstract).
Corgne, A., Schilling, M.E., Grégoire, M., Langlade, J., 2018. Experimental constraints on metasomatism of mantle wedge peridotites by hybridized adakitic melts. Lithos 308–309, 213–226.
Dan, M., O'Nions, R.K., 1995. The source regions of ocean island basalts. J. Petrol. 36, 133–159.
Falloon, T.J., Danyushevsky, L.V., 2000. Melting of refractory mantle at 1.5, 2 and 2.5 GPa under anhydrous and H_2O-undersaturated conditions: implications for the petrogenesis of high-Ca boninites and the influence of subduction components on mantle melting. J. Petrol. 41, 257–283.
Fu, H., Zhu, C., 1986. Ultra-high pressure measurement technology and experimental study on mantle minerals. Geol. Geochem. 14, 47–50 (in Chinese).
Gao, S., Takahashi, E., Suzuki, T., 2017. High-pressure melting experiments on basalt-peridotite layered source (KLB-1/N-MORB): implications for magma genesis in Hawaii. Int. J. Geosci. 8, 1–15.
Garcia, M.O., Presti, A.A., 1987. Glass in garnet pyroxenite xenoliths from Kaula Island, Hawaii: product of infiltration of host nephelinite. Geology 15, 904–906.
Genske, F.S., Beier, C., Haase, K.M., Turner, S.P., Krumm, S., Brandl, P.A., 2013. Oxygen isotopes in the Azores islands: crustal assimilation recorded in olivine. Geology 41, 491–494.
Green, T.H., Blundy, J.D., Adam, J., Yaxley, G.M., Austrheim, H., Griffin, W.L., 2000. SIMS determination of trace element partition coefficients between garnet, clinopyroxene and hydrous basaltic liquids at 2-7.5 GPa and 1080-1200 °C. Lithos 53, 165–187.
Hauri, E.H., 1996. Major-element variability in the Hawaiian mantle plume. Nature 382, 415–419.
Hill, E., Blundy, J.D., Wood, B.J., 2011. Clinopyroxene–melt trace element partitioning and the development of a predictive model for HFSE and Sc. Contrib. Mineral. Petrol. 161, 423–438.
Hilton, D.R., Barling, J., Wheller, G.E., 1995. Effect of shallow-level contamination on the helium isotope systematics of ocean-island lavas. Nature 373, 330–333.
Hofmann, A.W., 1997. Mantle geochemistry: the message from oceanic volcanism. Nature 385, 219–229.
Hofmann, A.W., White, W.M., 1982. Mantle plumes from ancient oceanic crust. Earth Planet Sci. Lett. 57, 421–436.
Huang, S.C., Zheng, Y.F., 2017. Mantle geochemistry: insights from ocean island basalts. Sci. China Earth Sci. 80, 1–25.
Huang, X.L., Xu, Y.G., Lo, C.H., Wang, R.C., Lin, C.Y., 2007. Exsolution lamellae in a clinopyroxene megacryst aggregate from Cenozoic basalt, Leizhou Peninsula, South China: petrography and chemical evolution. Contrib. Mineral. Petrol. 154, 691–705.
Jackson, M.G., Weis, D., Huang, S., 2012. Major element variations in Hawaiian shield lavas: source features and perspectives from global ocean island basalt (OIB) ststematic. G-cubed 13, Q09009.
Johnston, A.D., Wyllie, P.J., 1989. The system tonalite-peridotite-H_2O at 30 kbar, with applications to hybridization in subduction zone magmatism. Contrib. Mineral. Petrol. 102, 257–264.
Kelemen, P.B., Dick, H., Quick, J.E., 1992. Formation of harzburgite by pervasive melt/rock reaction in the upper mantle. Nature 358, 635–641.
Klemme, S., Blundy, J.D., Bernard, J., 2002. Experimental constraints on major and trace element partitioning during partial melting of eclogite. Geochem. Cosmochim. Acta 66, 3109–3123.

Lambart, S., Laporte, D., Provost, A., Schiano, P., 2012. Fate of pyroxenite-derived melts in the peridotitic mantle: thermodynamic and experimental constraints. J. Petrol. 53, 451–476.

Lambart, S., Laporte, D., Schiano, P., 2009. An experimental study of focused magma transport and basalt–peridotite interactions beneath mid-ocean ridges: implications for the generation of primitive MORB compositions. Contrib. Mineral. Petrol. 157, 429–451.

Liang, Y., Richter, F.M., Davis, A.M., Watson, E.B., 1996. Diffusion in silicate melts: I. Self diffusion in CaO-Al_2O_3-SiO_2 at 1500 °C and 1 GPa. Geochem. Cosmochim. Acta 60, 4353–4367.

Liu, J.-Q., Ren, Z.-Y., 2013. Diversity of source lithology and its identification for basalts: a case study of the Hainan basalts. Geotect. Metallogenia 37, 471–488 (in Chinese with English abstract).

Liu, Y., Hu, Z., Gao, S., Günther, D., Xu, J., Gao, C., Chen, H., 2008. In situ analysis of major and trace elements of anhydrous minerals by LA-ICP-MS without applying an internal standard. Chem. Geol. 257, 34–43.

Mallik, A., Dasgupta, R., 2012. Reaction between MORB-eclogite derived melts and fertile peridotite and generation of ocean island basalts. Earth Planet Sci. Lett. 329–330, 97–108.

Morgan, Z., Liang, Y., 2005. An experimental study of the kinetics of lherzolite reactive dissolution with applications to melt channel formation. Contrib. Mineral. Petrol. 150, 369–385.

Morimoto, N., 1988. Nomenclature of pyroxenes. Mineral. Petrol. 39, 55–76.

Niu, Y., 2009. Some basic concepts and problems on the petrogenesis of intra-plate ocean island basalts. Chin. Sci. Bull. 54, 4148–4160.

Pertermann, M., Hirschmann, M.M., 2003. Partial melting experiments on a MORB-like pyroxenite between 2 and 3 GPa: constraints on the presence of pyroxenite in basalt source regions from solidus location and melting rate. J. Geophys. Res.: Solid Earth 108, 2125.

Pertermann, M., Hirschmann, M.M., Hametner, K., Günther, D., Schmidt, M.W., 2004. Experimental determination of trace element partitioning between garnet and silica-rich liquid during anhydrous partial melting of MORB-like eclogite. G-cubed 5, Q05A01.

Putirka, K., Ryerson, F.J., Perfit, M., Ridley, W.I., 2011. Mineralogy and composition of the oceanic mantle. J. Petrol. 52, 279–313.

Qi, L., Jing, H., Gregoire, D.C., 2000. Determination of trace elements in granites by inductively coupled plasma mass spectrometry. Talanta 51, 507–513.

Rapp, R.P., Norman, M.D., Laporte, D., Yaxley, G.M., Martin, H., Foley, S.F., 2010. Continent formation in the Archean and chemical evolution of the cratonic lithosphere: melt–rock reaction rxperiments at 3–4 GPa and petrogenesis of Archean Mg-diorites (Sanukitoids). J. Petrol. 51, 1237–1266.

Rapp, R.P., Shimizu, N., Norman, M.D., Applegate, G.S., 1999. Reaction between slab-derived melts and peridotite in the mantle wedge experimental constraints at 3.8 GPa. Chem. Geol. 160, 335–356.

Ravna, E.K., 2000. Distribution of Fe^{2+} and Mg between coexisting garnet and hornblende in synthetic and natural systems: an empirical calibration of the garnet–hornblende Fe^{2+}–Mg geothermometer. Lithos 53, 265–277.

Ren, Z.Y., Hanyu, T., Miyazaki, T., Chang, Q., Kawabata, H., Takahashi, T., Hirahara, Y., Nichols, A.R.L., Tatsumi, Y., 2009. Geochemical differences of the Hawaiian shield lavas: implications for melting process in the heterogeneous Hawaiian plume. J. Petrol. 50, 1553–1573.

Salters, V.J.M., Longhi, J., 1999. Trace element partitioning during the initial stages of melting beneath mid-ocean ridges. Earth Planet Sci. Lett. 166, 15–30.

Sébastien, P., Baker, M.B., Stolper, E.M., 2008. Metasomatized lithosphere and the origin of alkaline lavas. Science 320, 916–919.

Sen, G., 1988. Petrogenesis of spinel lherzolite and pyroxenite suite xenoliths from the Koolau shield, Oahu, Hawaii: implications for petrology of the post-eruptive lithosphere beneath Oahu. Contrib. Mineral. Petrol. 100, 61–91.

Shaw, C.S.J., Dingwell, D.B., 2007. Experimental peridotite–melt reaction at one atmosphere: a textural and chemical study. Contrib. Mineral. Petrol. 155, 199–214.

Shaw, C.S.J., Thibault, Y., Edgar, A.D., Lloyd, F.E., 1998. Mechanisms of orthopyroxene dissolution in silica-undersaturated melts at 1 atmosphere and implications for the origin of silica-rich glass in mantle xenoliths. Contrib. Mineral. Petrol. 132, 354–370.

Sobolev, A.V., Hofmann, A.W., Kuzmin, D.V., Yaxley, G.M., Arndt, N.T., Chung, S.-L., Danyushevsky, L.V., Elliott, T., 2007. The amount of recycled crust in sources of mantle-derived melts. Science 316, 412–417.

Sobolev, A.V., Hofmann, A.W., Nikogosian, I.K., 2000. Recycled oceanic crust observed in 'ghost plagioclase' within the source of Mauna Loa lavas. Nature 404, 986–990.

Sobolev, A.V., Hofmann, A.W., Sobolev, S.V., Nikogosian, I.K., 2005. An olivine-free mantle source of Hawaiian shield basalts. Nature 434, 590–603.

Stolper, E., Sherman, S., Garcia, M., Maker, M., Seaman, C., 2004. Glass in the submarine section of the HSDP2 drill core. G-cubed 5, Q07G15.

Stracke, A., Tipper, E.T., Klemme, S., Bizimis, M., 2018. Mg isotope systematics during magmatic processes: inter-mineral fractionation in mafic to ultramafic Hawaiian xenoliths. Geochem. Cosmochim. Acta 226, 192–205.

Sun, S.S., Mcdonough, W.F., 1989. Chemical and isotopic systematics of oceanic basalts: implications for mantle composition and processes. Geol. Soc. Lond. Special Publ. 42, 313–345.

Tegner, C., Wilson, J.R., Robins, B., 2005. Crustal assimilation in basalt and jotunite: constraints from layered intrusions. Lithos 83, 299–316.

Tingle, T.N., Green, H.W., Young, T.E., Koczynski, T.A., 1993. Improvements to Griggs-type apparatus for mechanical testing at high pressures and temperatures. Pure Appl. Geophys. 141, 523–543.

Tominaga, A., Kato, T., Kubo, T., Kurosawa, M., 2009. Preliminary analysis on the mobility of trace incompatible elements during the basalt and peridotite reaction under uppermost mantle conditions. Phys. Earth Planet. In. 174, 50–59.

Tuff, J., Gibson, S.A., 2007. Trace-element partitioning between garnet, clinopyroxene and Fe-rich picritic melts at 3 to 7 GPa. Contrib. Mineral. Petrol. 153, 369–387.

Van Den Bleeken, G., Müntener, O., Ulmer, P., 2011. Melt variability in percolated peridotite: an experimental study applied to reactive migration of tholeiitic basalt in the upper mantle. Contrib. Mineral. Petrol. 161, 921–945.

Wagner, T.P., Grove, T.L., 1998. Melt/harzburgite reaction in the petrogenesis of tholeiitic magma from Kilauea volcano, Hawaii. Contrib. Mineral. Petrol. 131, 1–12.

Wang, C., Jin, Z.M., Gao, S., Zhang, J.F., Zheng, S., 2010. Eclogite-melt/peridotite reaction: experimental constrains on the destruction mechanism of the North China Craton. Sci. China Earth Sci. 53, 797–809.

Wang, C., Liang, Y., Dygert, N., Xu, W., 2016. Formation of orthopyroxenite by reaction between peridotite and hydrous basaltic melt: an experimental study. Contrib. Mineral. Petrol. 171, 77 https://doi.org/10.1007/s00410-016-1287-z.

Wang, C., Liang, Y., Xu, W., Dygert, N., 2013. Effect of melt composition on basalt and peridotite interaction: laboratory dissolution experiments with applications to mineral compositional variations in mantle xenoliths from the North China Craton. Contrib. Mineral. Petrol. 166, 1469–1488.

Wang, M., Tang, H., 2013. Reaction experiments between tonalitic melt and mantle olivine and their implications for genesis of high-Mg andesites within cratons. Sci. China Earth Sci. 56, 1918–1925.

Wang, M., Zang, C., Tang, H., 2019. The effect of P–T on the reaction between tonalitic melt and mantle lherzolite at 2–4 GPa and implications for evolution of North China Cratonic lithosphere and generation of high Mg# andesite. Lithos 324–325, 626–639.

Westrenen, W.V., Draper, D.S., 2007. Quantifying garnet-melt trace element partitioning using lattice-strain theory: new crystal-chemical and thermodynamic constraints. Contrib. Mineral. Petrol. 154, 717–730.

Wim, V., Westrenen, Jon, B., Bernard, W., 1999. Crystal-chemical controls on trace element partitioning between garnet and anhydrous silicate melt. Am. Mineral. 84, 838–847.

Wood, B.J., Trigila, R., 2001. Experimental determination of aluminous clinopyroxene–melt partition coefficients for potassic liquids, with application to the evolution of the Roman province potassic magmas. Chem. Geol. 172, 213–223.

Xiao, L., Xu, Y.G., Mei, H.J., Zheng, Y.F., He, B., Pirajno, F., 2004. Distinct mantle sources of low-Ti and high-Ti basalts from the western Emeishan large igneous province, SW China: implications for plume lithosphere interaction. Earth Planet Sci. Lett. 228, 525–546.

Xiong, X., Han, J., 2007. Phase equilibrium and trace element partitioning between minerals and melt in the metabasalt system: constraints on the formation conditions of TTG/adakite magmas and the growth of early continental crust. Earth Sci. Front. 14, 149–158 (in Chinese with English abstract).

Xu, Y., Chung, S.L., Jahn, B.M., Wu, G., 2001. Petrologic and geochemical constraints on the petrogenesis of Permian–Triassic Emeishan flood basalts in southwestern China. Lithos 58, 145–168.

Xu, Y.G., He, B., Chung, S.L., Menzies, M.A., Frey, F.A., 2004. Geologic, geochemical, and geophysical consequences of plume involvement in the Emeishan flood-basalt province. Geology 32, 917–920.

Yaxley, G.M., Green, D.H., 1998. Reactions between eclogite and peridotite: mantle refertilisation by subduction of oceanic crust. Schweizer. Mineral. Petrogr. Mitteil. 78, 243–255.

Zindler, A., Hart, S.R., 1986. Chemical geodynamics. Annu. Rev. Earth Planet Sci. 14, 493–571.